



Tungsten-Steel Functionally Graded Coatings for Nuclear Fusion Applications Manufactured by Cold Gas Spraying

Georg Mauer¹ · Karl-Heinz Rauwald¹ · Yoo Jung Sohn¹

Submitted: 5 July 2022 / in revised form: 7 November 2022 / Accepted: 13 November 2022 / Published online: 2 December 2022
© The Author(s) 2022

Abstract In nuclear fusion reactors, the first wall is the name given to the surface which is in direct contact with the plasma. A part of it is the divertor which is a device that removes fusion products from the plasma and impurities that have entered into it from the vessel lining. It is covered with water cooled tiles which have to withstand high temperatures and high heat fluxes. Moreover, resistance to neutron bombardment, low tritium absorption and low hydrogen permeation are additional demands. One materials concept under research is the application of a Reduced Activation Ferritic Martensitic Steel (RAFM) as a structural material with a tungsten protective coating. Since there is a considerable thermal mismatch between, a functional-graded materials concept was proposed.

As the formation of undesired intermetallic Fe-W phases as well as oxidation should be avoided, cold gas spraying was chosen as manufacturing process. Two powder blends of EUROFER97 RAFM steel and a fine

tungsten powder cut on the one hand and a coarser one on the other hand were tested in different ratios. The coatings were characterized with respect to their porosity and surface structure. Furthermore, the deposition efficiencies for steel and tungsten were determined each. It turned out that the deposition process is a complex mixed situation of bonding and erosion mechanisms as the deposition windows of these very different materials obviously diverge. Thus, a lower working gas temperature and pressure was advantageous in some cases. Unexpectedly, the coarser tungsten powder in general enabled to achieve better results.

Keywords cold gas dynamic spraying · feedstock · nuclear fusion · processing · tungsten

Introduction

Nuclear fusion is aimed at replicating the fusion processes of the sun to deliver energy. The most feasible reaction is fusing the two hydrogen's isotopes deuterium and tritium. This reaction releases a large amount of energy, three-quarters of which is carried away by the neutrons produced by it (Ref 1). Currently, the most powerful facilities for the development of fusion technology are based on the Tokamak principle. Therein, a powerful magnetic field is used to confine plasma in the shape of a torus. ITER (International Thermonuclear Experimental Reactor) in Cadarache, France, will be the world's largest magnetic confinement plasma physics experiment and Tokamak system (Ref 1). It is designed to generate more heat than used to start the fusion reaction.

Fusion projects like ITER integrate much of the science and technology knowledge and expertise which has been

This article is an invited paper selected from presentations at the 2022 International Thermal Spray Conference, held May 4–6, 2022 in Vienna, Austria, and has been expanded from the original presentation. The issue was organized by André McDonald, University of Alberta (Lead Editor); Yuk-Chiu Lau, General Electric Power; Fardad Azarmi, North Dakota State University; Filofteia-Laura Toma, Fraunhofer Institute for Material and Beam Technology; Heli Koivuluoto, Tampere University; Jan Cizek, Institute of Plasma Physics, Czech Academy of Sciences; Emine Bakan, Forschungszentrum Jülich GmbH; Šárka Houdková, University of West Bohemia; and Hua Li, Ningbo Institute of Materials Technology and Engineering, CAS.

✉ Georg Mauer
g.mauer@fz-juelich.de

¹ Institute of Energy and Climate Research, IEK-1: Materials Synthesis and Processing, Forschungszentrum Jülich GmbH, Jülich, Germany

developed over a period of several decades. The all-metal plasma facing components (PFCs) are among others key developments almost completely covering the internal surface of the reactor's vacuum vessel and representing the physical interface between the thermonuclear plasma and the rest of the device (Ref 2). In a Tokamak type reactor, the PFCs comprise two main systems: the blanket system (this includes the plasma facing so-called first wall) and the divertor (Ref 3), which removes fusion products from the plasma and impurities that have entered into it from the vessel lining. They are both mechanically attached to the vacuum vessel and have to remove the thermal power. This is achieved by actively cooling via highly sub-cooled pressurized water (Ref 2).

There are important requirements on PFC material candidates (Ref 4):

- High temperatures up to 1,000 °C;
- High heat fluxes up to 5 MW m⁻² (blanket) and 10–20 MW m⁻² (divertor);
- Resistance to neutron bombardment, low tritium absorption;
- No long-living radioactive isotopes must be formed as a result of neutron irradiation;
- Low hydrogen permeation.

Reduced activation ferritic martensitic (RAFM) steel is the primary choice material for first wall and blanket structural application. These steels have been developed in order to simplify special waste storage of highly radioactive structures of fusion reactor after service (Ref 5). With this objective some alloying elements such as Mo, Nb and Ni present in the commercial martensitic steels have been replaced by other elements which exhibit faster decay of induced radioactivity such as Ta, W and V (Ref 6). EUROFER97 (9CrWVTa) is the reference RAFM steel developed for the requirements of the European fusion technology program (Ref 7).

For protecting first wall and divertor materials (the divertor has to withstand the highest thermal loads among all of the PFCs) from physical and chemical sputtering by plasma particles and surface blistering, tungsten is considered as an obvious armor material due to its advantageous properties (Ref 4):

- High melting point (3,422 °C), low vapor pressure;
- High creep resistance, high temperature strength;
- Good thermal conductivity;
- Good erosion resistance;
- Low hydrogen permeability.

Plasma spraying is a potential technology to fabricate such protective layers. Matějček et al. used a water-stabilized plasma torch (WSP) to deposit tungsten and martensitic stainless steel AISI 410 (X12Cr13) coatings

(Ref 8). They identified the spray distance and the substrate temperature as significant process parameters. Spraying into a shrouding chamber flushed with an argon–hydrogen mixture allowed to increase the substrate temperature up to 715 °C. While porosity, hardness and thermal conductivity improved at increasing temperatures due to enhanced intersplat bonding and coating density, oxidation turned out to be an issue. Although the water-stabilized plasma itself is a reducing environment, there is a strong entrainment of ambient air leading to in-flight oxidation (Ref 9) as tungsten oxidizes rapidly already above approx. 400 °C.

Since there is a substantial thermal mismatch between steel and tungsten (the coefficient of thermal expansion for EUROFER97 is 12.7 vs. 4.4·10⁻⁶ K⁻¹ for tungsten), the application of a functionally graded material (FGM) concept is an obvious solution. FGMs sprayed with the mentioned WSP torch into a shrouding chamber showed promising mechanical and thermo-physical properties as well as a thermal conductivity in the range of the EUROFER97 steel (Ref 10). However, at substrate preheating temperatures beyond 700 °C, the formation of intermetallic precipitates (λ -phase Fe₂W and μ -phase Fe₇W₆) during deposition was observed. This was supposed to be a limiting factor when trying to improve thermal conductivity and ductility by increasing the process temperature. A subsequent study (Ref 11) was focused on the improvement in density and thermal conductivity. Here, inert gas shrouding was applied through a shielding tube attached to the front panel of the torch, enclosing the nozzle together with the anode. In addition, hot isostatic pressing (HIP) was tried as an optional technique to improve the density and thermal conductivity of the coatings.

The low pressure plasma spraying process (LPPS), often referred to as vacuum plasma spraying (VPS), was also used to manufacture EUROFER97-tungsten FGMs. Emmerich et al. reported that the limited temperature window during LPPS must be complied with to achieve good coating adhesion on the one hand while on the other hand exceeding the tempering temperature of the steel must be avoided (Ref 12, 13). Vaßen et al. produced graded structures via LPPS consisting of up to five layers with different tungsten-steel compositions plus two pure steel and tungsten layers (Ref 14). The huge difference in the melting point of tungsten and steel could be compensated in the thermal spray process by adjusting particle sizes and injection conditions.

As the process temperature turned out to be always an issue needing special attention, cold gas spraying (CGS) appears as a potential alternative to plasma spraying because of the relatively low process temperatures (Ref 15). By CGS, Cizek et al. (Ref 16) processed blended mixtures of tungsten with Al 6060 alloy (AlMgSi0.5), AISI 304 stainless steel (X5CrNi18-10), unalloyed tempering

steel C45E as well as tungsten mechanically alloyed with Cr and then blended with Ti. The tungsten content of the feedstocks ranged between 83 and 95 wt.%. They even succeeded in cold gas spraying an 80 µm pure tungsten coating on Al 6060 without any other metallic matrix material.

In this work, CGS was tried to produce tungsten-steel FGMs. Two powder blends of EUROFER97 steel and a fine tungsten powder cut on the one hand and a coarser one on the other hand were tested in different ratios. The coatings were characterized with respect to their porosity and composition. Furthermore, the deposition efficiencies (DE) for steel and tungsten were determined each. The results provide insight into the complex deposition mechanisms and give indications for the choice of suitable deposition parameters.

Experimental Methods and Procedures

The EUROFER97 reduced activation ferritic martensitic (RAFM) steel powder (NANOVAL GmbH & Co. KG, Berlin, Germany) had the nominal composition of 9% Cr, 1.1% W, 0.2% V, 0.12% Ta, and 0.11% C. The sieve fraction was −52 µm. The particle size distribution was measured by laser diffractometry (Horiba LA950, Retsch Technology GmbH, Haan, Germany). Table 1 gives the characteristic diameters and densities. Two tungsten powders were used. The coarser one was a sintered cut −25/+5 µm AMPERIT® 140.071 (Höganäs, formerly H.C. Starck GmbH, Laufen/Goslar, Germany). The finer powder cut −10 µm was agglomerated (Global Tungsten & Powders Corp., Towanda PA, USA). Table 1 gives the characteristic particle diameters and densities. Figure 1 shows the tungsten powders.

Spray experiments were carried out on an Impact cold spray system 5/11 (Impact Innovations GmbH, Haun/Rattenkirchen, Germany) equipped with a standard D24 de-Laval type converging–diverging nozzle with an expansion ratio of 5.6 mounted on a six axis robot. Nitrogen was used as propellant and feedstock carrier gases. The cold spray system allowed a maximum gas temperature of 1100 °C (measured immediately before the gas enters the nozzle, opposite to powder injection) at a maximum inlet pressure

of 5 MPa. Two working gas conditions were selected for the experiments, 950 °C/4 MPa and 1100 °C/5 MPa. Increasing both parameters, gas temperature and pressure, principally causes higher particle velocities, with the temperature showing the greater effect. The range limits of useful pressures and temperatures are the particle velocity falling below the critical velocity on the one hand and exceeding the erosion velocity on the other hand. For the two combinations of temperature and pressure chosen here, particle velocities were expected to lie in between, i.e., in the so-called window of deposition.

After some preliminary tests, the spray distance from the nozzle exit to the substrate surface was set to 60 mm. The spray angle was 90°. The gun travel speed for the coating deposition was varied between 125 and 500 mm/s. The raster step was 1 mm and the number of deposition passes was varied between 5 and 20. Two powder feeders, one for the steel powder and one for a tungsten feedstock, were connected by a Y-shape tube with the gun. Different steel-tungsten ratios in the blend were obtained by adjusting the two powder feed rates, thereby keeping the total powder volume feed rate through both lines constantly at 5.936 cm³/min. As the powders in the feeder are compacted by vibration they are assumed to have tap density. The carrier gas flow was 3 m³/h in each feed line. The powder mixture was injected in radial direction in the pre-chamber of the gun where it is heated before being accelerated by the working gas in the convergent-divergent nozzle.

Austenitic steel substrates (AISI 304) were grit blasted with corundum (−600/+420 µm) and cleaned in an ultrasonic bath. DEs were determined on the basis of the powder mass feed rate, sample area, gun motion, and coating weight considering only the spray time when the gun is over the sample and thus excluding over-spraying, Eq. 1:

$$DE = \frac{m_c s v_t}{\dot{m} A c} \quad (\text{Eq. 1})$$

where m_c is the coating mass (difference of sample masses before and after coating), s is the raster step, v_t is the gun travel velocity, \dot{m} is the powder mass feed rate (estimated by the volumetric powder feed rate and the powder tap densities), A is the substrate area, and c the number of passes. The DEs for steel and tungsten can be determined

Table 1 Characteristic data of spray powders

	EUROFER97 steel	Tungsten, coarse	Tungsten, fine
d ₁₀ (µm)	8.2	7.4	4.7
d ₅₀ (µm)	16.4	13.4	7.7
d ₉₀ (µm)	37.7	23.3	12.0
Bulk density (g/cm ³)	4.255	7.144	8.343
Tap density (g/cm ³)	4.985	9.050	9.953

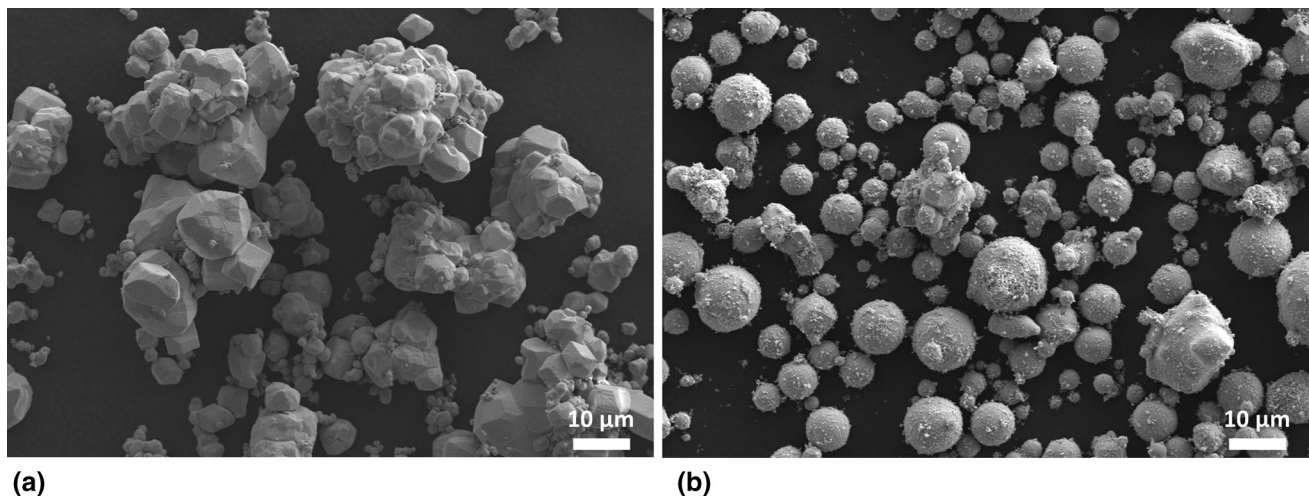


Fig. 1 Tungsten powders; a) coarse cut, b) fine cut (secondary electron images)

individually by inserting the individual mass feed rates \dot{m}_{St} and \dot{m}_W as well as the mass fractions in the coatings of tungsten $m_{c,W}$ and steel $m_{c,St}$. They can be obtained from cross-sectional micrographs, Eq. 2 and 3:

$$m_{c,W} = \frac{m_c}{1 + \frac{V_{V,St}\rho_{St}}{V_{V,W}\rho_W}} \quad (\text{Eq. 2})$$

$$m_{c,St} = \frac{m_c}{1 + \frac{V_{V,W}\rho_W}{V_{V,St}\rho_{St}}} \quad (\text{Eq. 3})$$

where the density of the steel and tungsten is $\rho_{St} = 7.75 \text{ g/cm}^3$ and $\rho_W = 19.29 \text{ g/cm}^3$, respectively; $V_{V,St}$ and $V_{V,W}$ are the volume fractions of steel and tungsten in the coating. Delesse's stereologic¹ principle of equality of volume, area and linear fractions of microstructural constituents (Ref 17, 18) says:

- The estimate of A_A on unbiased sections will be an unbiased estimate of V_V ;
- The estimate of V_V is independent of the shape of the sample and the constituent's shape and distribution;

with $A_A = A_m / A_t$, where A_m is the measured cross-sectional area of the considered constituent obtained by planimetry, and A_t the total measured sample area. Thus, $V_{V,St}$ and $V_{V,W}$ can be equated with the area fractions $A_{A,St}$ and $A_{A,W}$ in the transverse sections, respectively. Planimetry was carried out by digital image analysis of cross-sectional SEM micrographs using the public ImageJ software (Ref 19). 4–6 images per sample were evaluated to validate the results statistically. Since there was a sufficient material contrast in the back-scattered electron

micrographs, steel and tungsten could be well distinguished while excluding pores and voids reliably.

Scanning electron microscope investigations (SEM) were accomplished by an Ultra55 model (Carl Zeiss NTS GmbH, Oberkochen, Germany) combined with an energy-dispersive x-ray INCAEnergy355 spectrometer (EDS, Oxford Instruments Ltd., Abingdon, Oxfordshire, UK). For SEM examination, the samples were coated with approximately 2 nm platinum. EDS point analyses were performed with an acceleration voltage of 15 kV.

For surface topographic measurements, a non-contact optical inspection system CT 350 T (cyberTECHNOLOGIES GmbH, Eching-Dietersheim, Germany) with a 300 mm x-y-scanning stage (lateral resolution 50 nm) was used in connection with a CHR 3000 confocal chromatic white light sensor (measurement range 3000 µm, resolution 0.10 µm, spot size 12 µm, step size 50 µm × 20 µm). Data were acquired at a rate of 2–4 kHz.

Phase analyses by x-ray diffractometry were carried out by means of the Empyrean system (Malvern Panalytical GmbH, Kassel, Germany) applying the focusing Bragg–Brentano (BB) geometry. All XRD scans were taken using Cu-K α radiation (45 kV, 40 mA) at Bragg angles 2θ between 30° and 90°, with increments of 0.026° and a scan time of 1 s/step. Thereafter, the data were analyzed using the TOPAS software V4.2 (General profile and structure analysis software for powder diffraction data, Bruker AXS, Karlsruhe, Germany).

Results and Discussion

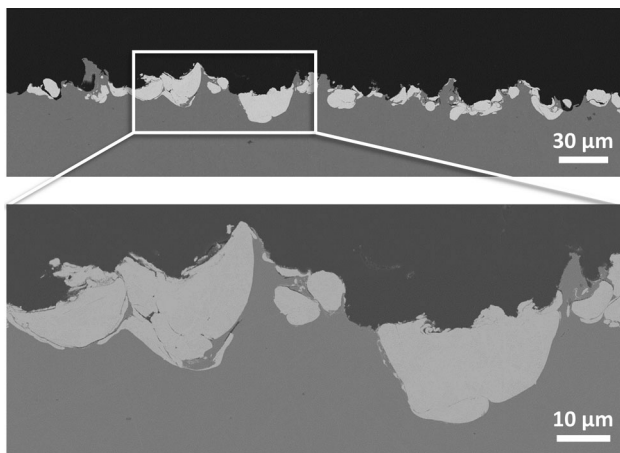
Coating Microstructures

Seven different powder blends were used, Table 2. The attempt to deposit a pure tungsten coating from the finer cut

¹ Stereology deals with the relationship between sections through three-dimensional geometric bodies and the bodies themselves, and provides mathematical relationships between measured quantities on the two-dimensional section and the three-dimensional nature of the microstructural constituents.

Table 2 Composition of the sprayed tungsten-steel blends; the percentages refer to the totally fed powder volume

	EUROFER97 steel	Tungsten
Tungsten fine $-10\ \mu\text{m}$	0%	100%
	25%	75%
	50%	50%
	75%	25%
Tungsten coarse $-25/+5\ \mu\text{m}$	25%	75%
	50%	50%
	75%	25%

**Fig. 2** Coating deposited from 100% fine tungsten powder ($-10\ \mu\text{m}$) at $1100\ ^\circ\text{C}$ and 5 MPa; back-scattered electron images

at maximum temperature and pressure ($1100\ ^\circ\text{C}$ and 5 MPa) was not successful, Fig. 2. Although there are some tungsten particles bonded to the substrate, also strong erosion took place so that the final weight of the sprayed sample was smaller than the initial weight of the uncoated one. The tungsten-steel interface resembles to the pure tungsten coating shown in (Ref16). It might have been possible to continue spraying for a longer time to obtain a similar result; however, this was not undertaken in this work because of the very poor DE.

In Fig. 3, cross sections are given of tungsten-steel coatings sprayed at $950\ ^\circ\text{C}$ and 4 MPa using three different feedstock compositions with the fine and the coarse tungsten powder each. It is obvious that the DE decreased as the tungsten fraction was increased. Besides, it was generally smaller if the fine tungsten powder was used. For the large tungsten content, it is evident that the cohesion of the coatings was insufficient.

In Fig. 4, cross sections are given of tungsten-steel coatings sprayed at $1100\ ^\circ\text{C}$ and 5 MPa using three

different feedstock compositions with the fine and the coarse tungsten powder, respectively. In one case, the coating spalled off some hours after spraying indicating large residual stresses. The DE increases generally due to the higher temperature and pressure while the trends are consistent with the results for $950\ ^\circ\text{C}$ and 4 MPa. For 75%W, the coatings show an improved cohesion compared to the lower temperature and pressure, however, pores and voids are still obvious for the fine tungsten powder. For 25% and 50%W with the fine tungsten powder, the cross sections show basically a deposition in twenty layers resulting from the twenty coating passes.

One sample was sprayed exceptionally in five passes with a low gun travel velocity of 125 mm/s, Fig. 5, while all the other experiments had been done in twenty cycles with 500 mm/s. The feedstock was 50% steel and 50% of the fine tungsten powder. Here, the single coating layers resulting from each deposition pass are even more pronounced than in the sample shown in Fig. 4 at the bottom left. Obviously, the (bright in SEM image) tungsten particles are concentrated in the middle of each layer. It is suggested that the tungsten particles concentrate in the core of the particle jet, while more steel particles are traveling at the edges.

Porosities

In Fig. 6, the porosities determined by digital image analysis are given quantitatively for the same samples. The lowest porosities are achieved with the coarse tungsten powder, the higher gas temperature and pressure, as well as with the medium and highest steel content. The minima at 50%W/50%St are assumed to result from a peening effect on the one hand increasing at larger tungsten content, and the better particle bonding on the other hand at higher steel content.

Coating Surfaces

Besides the coating cross sections, also the surfaces show a more or less pronounced periodicity. The measurement results of some coating topographies are shown in Fig. 7. It is obvious that such waviness is related to the gun movement and the raster step size, which was 1 mm in all investigated cases. However, the wavelengths are in the 2 mm range here. This could indicate an interference between two periodicities, one resulting from the torch meander movement and the other induced by the radial tungsten and steel particle distribution in the spray jet. It seems reasonable to assume that the tungsten particles are more concentrated in the plume center, cp Section “Coating Microstructures”. In any case, the waviness of the concentration profile indicates that the two powders were

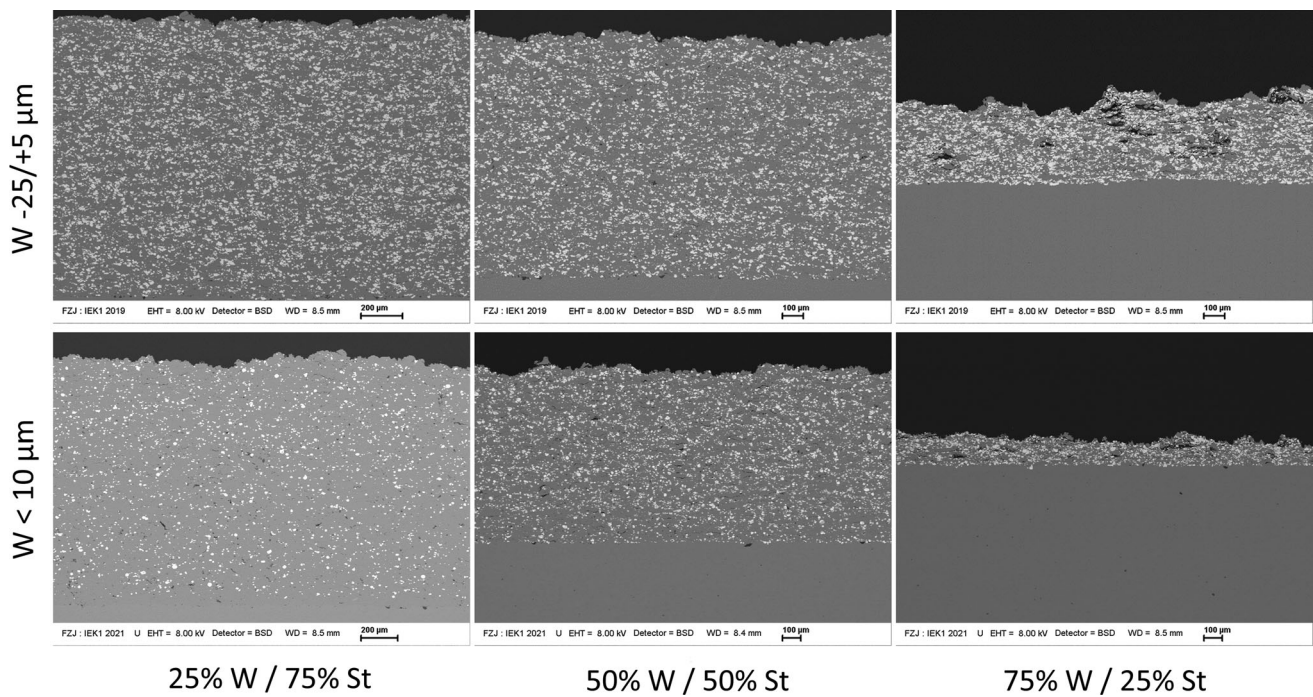


Fig. 3 Tungsten-steel coatings sprayed at 950 °C and 4 MPa using three different feedstock compositions with the fine (top row) and the coarse (bottom row) tungsten powder, respectively; back-scattered electron images

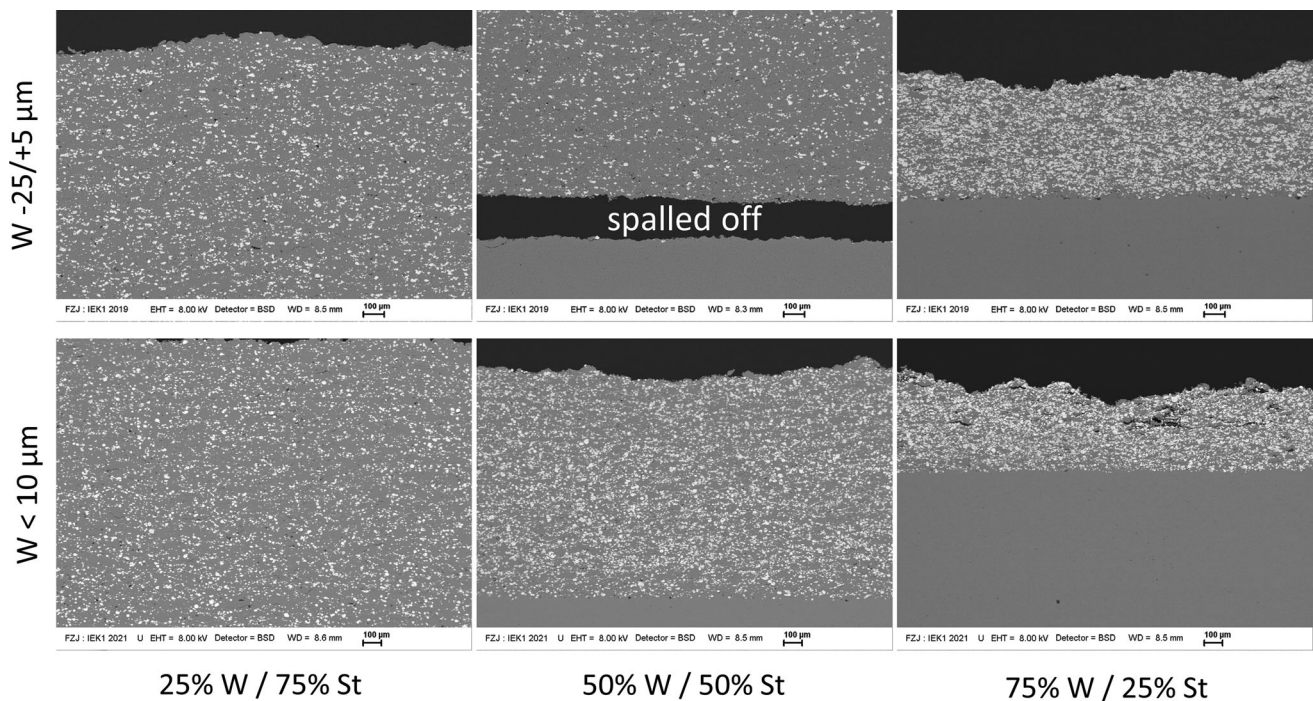


Fig. 4 Tungsten-steel coatings sprayed at 1100 °C and 5 MPa using three different feedstock compositions with the fine (top row) and the coarse (bottom row) tungsten powder, respectively; back-scattered electron images

not mixed uniformly at the impact. The waviness is more pronounced for the low tungsten contents of the powders while the profile heights are larger for the coarse tungsten powder.

The tungsten-steel ratios on the wavy coating surfaces differ at peak and valley positions. The XRD-irradiated area was 15 mm long and the average width was about 2 mm depending on the 2θ position. The 15 mm length

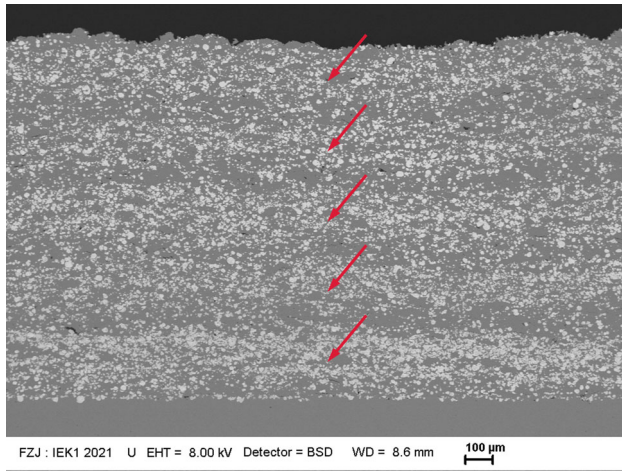
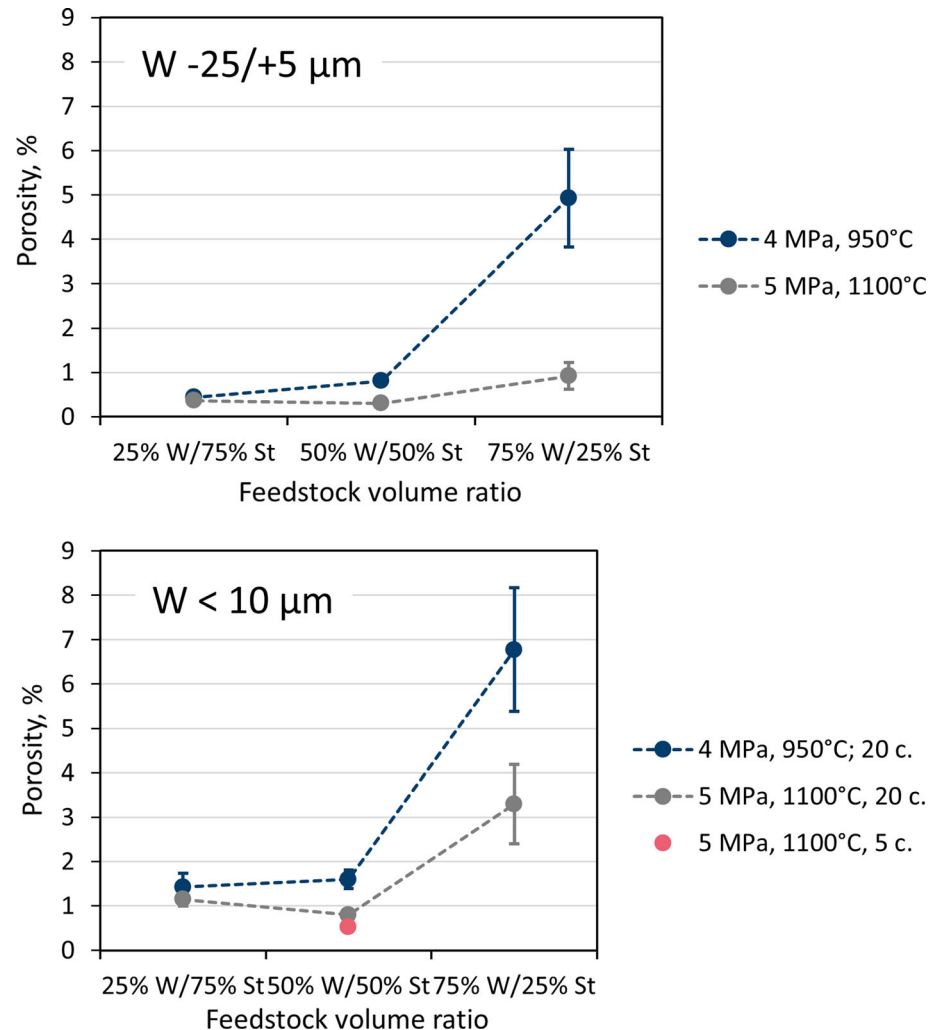


Fig. 5 Cross section of a coating sprayed in five passes with reduced gun travel speed at 1100 °C and 5 MPa with the fine tungsten powder (50% W + 50% St); the five resulting coating layers are marked with arrows (back-scattered electron image)

Fig. 6 Comparison of porosities for the coarse and fine tungsten powder as well as for two gas temperatures and pressures; error bars represent the uncertainties estimated from the analysis of 4–6 SEM images



was aligned parallel to the waviness of the sample surface. Figure 8 shows the XRD analyses of four peak and four valley positions. Both groups of diffractograms show a distinct difference between the background intensities. In principle, the background intensity is influenced by fluorescence of those metals which are positioned closely to the used x-ray anode material in the periodic table. As Cu-K α radiation was used in this work, a higher background intensity suggests a higher iron content rather than tungsten. This was found at the valley positions and was confirmed qualitatively by Rietveld refinements. However, their quantitative accuracy was limited due to the low local resolution. EDS was not applicable as an alternative method due to the high surface roughness of the samples (the analytic working distance cannot be maintained, correction factors cannot be determined properly, and shading and absorption may occur).

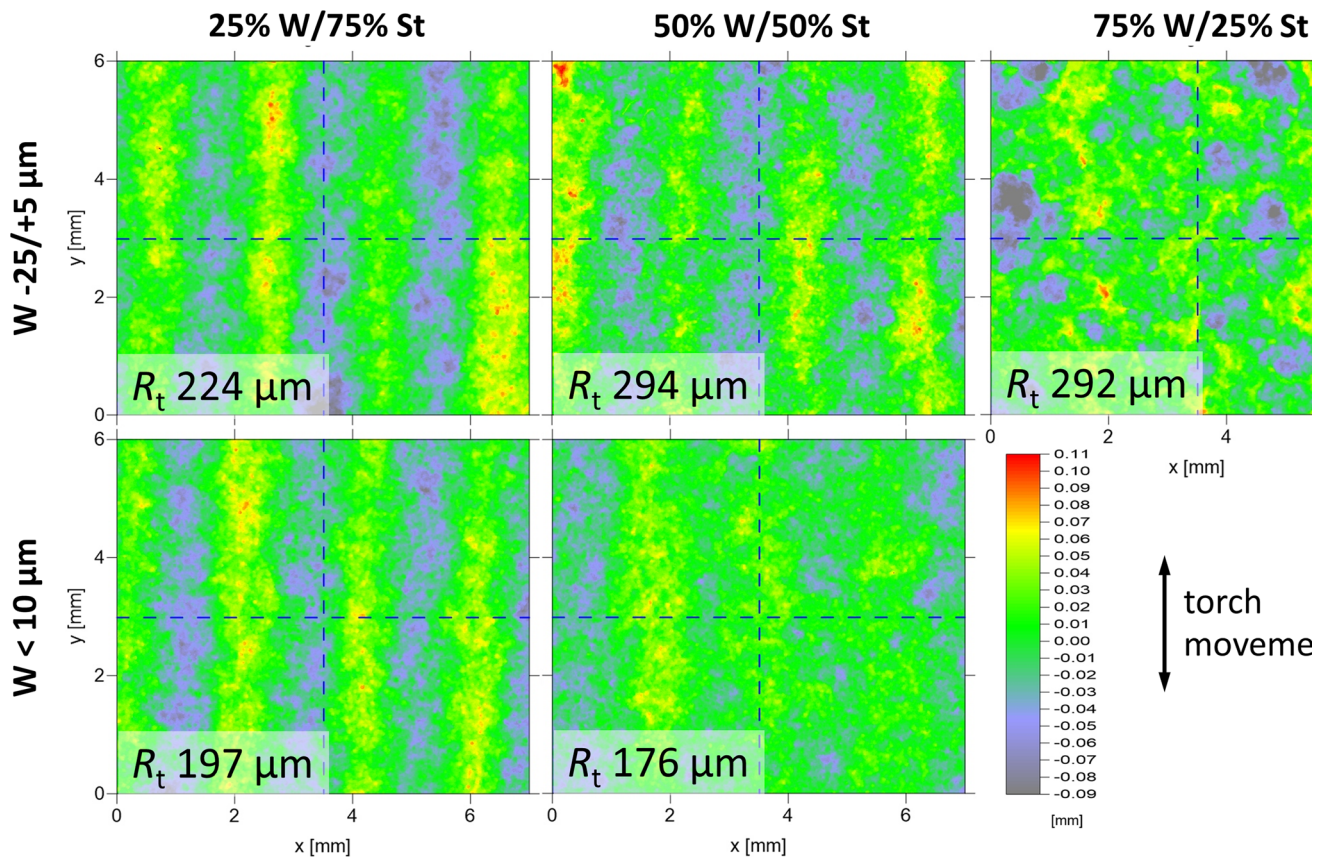
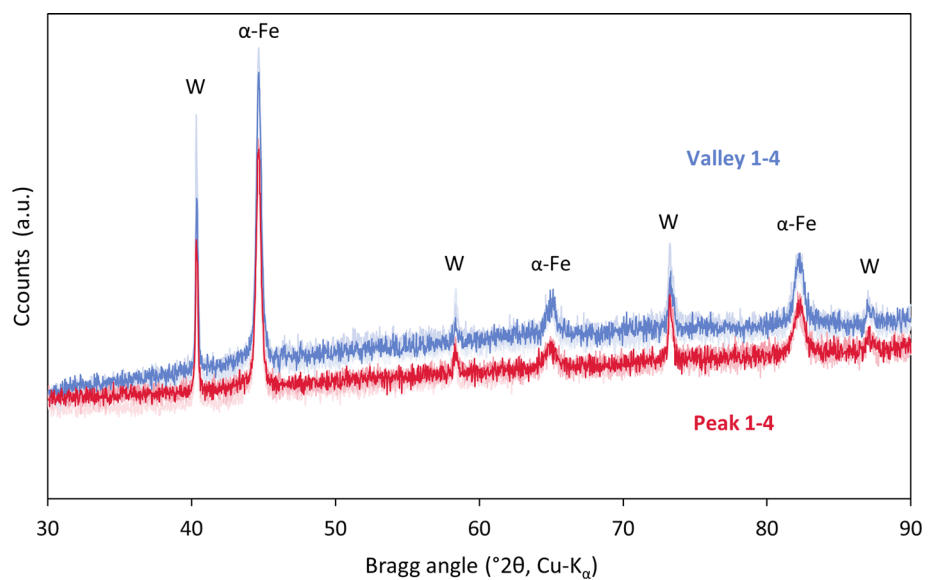


Fig. 7 Topographic measurements of sample surfaces with different feedstock compositions containing the coarse and the fine tungsten powder, respectively (5 MPa, 1100 °C); R_t indicates the total profile height

Fig. 8 XRD analyses of four peak and four valley positions on the wavy coating surface of the sample sprayed at 5 MPa and 1100 °C with the coarse powder (25%W, 75% St)



These results suggest that erosion is a considerable mechanism occurring in coincidence with deposition and peening. Obviously, there is a complex interaction between tungsten particle size and flow density on the one hand and

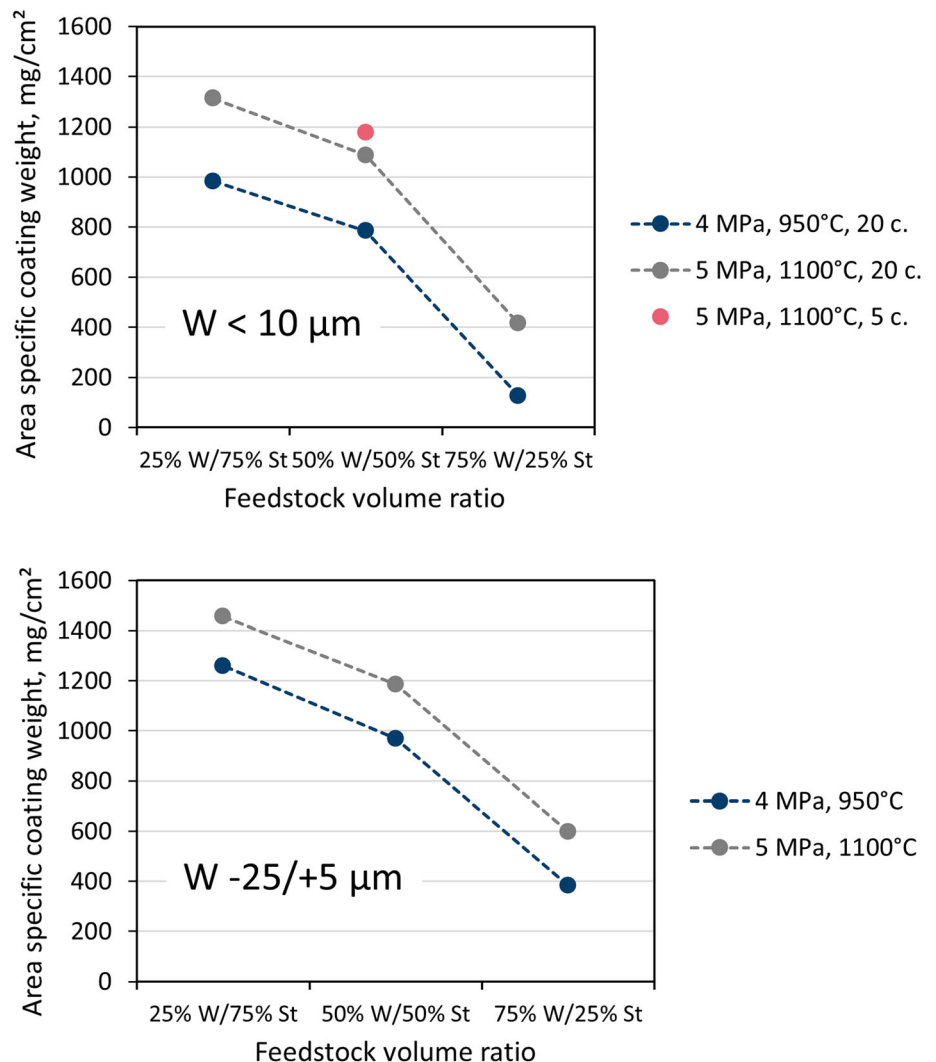
the specific deposition efficiencies of tungsten and steel on the other hand, see Section “[Deposition Efficiencies](#)”. It also seems to play a role how much steel is exposed at the coating surface providing a good attack for erosion by

tungsten particles, while already deposited tungsten spots locally enhance erosion resistance.

Area-Specific Coating Weights

The qualitative trends of the DE mentioned above in context with the coating cross sections in Fig. 3 and 4 are reflected quantitatively by the area-specific coating weights, Fig. 9. The sample which was sprayed exceptionally in five passes with a low gun travel velocity of 125 mm/s, while all the other experiments were done in twenty cycles with 500 mm/s, is represented by the red data point. The effect is obviously small. In general, the highest deposition rates were achieved for the coarse powder, the higher gas pressure and temperature as well as for the highest steel content.

Fig. 9 Comparison of area-specific coating weights for the coarse and fine tungsten powder as well as for two gas temperatures and pressures; the error due to the limited resolution of the scale is estimated to be $< 0.8 \text{ mg/cm}^2$

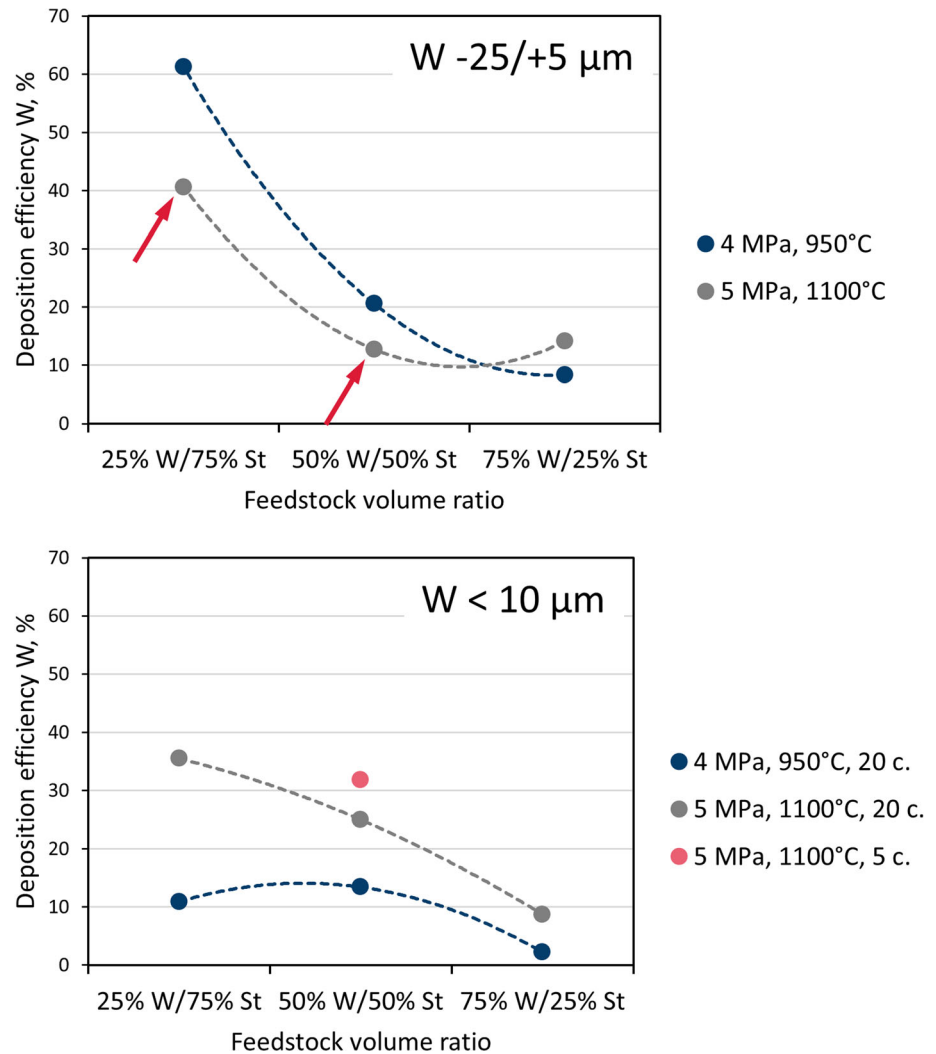


Deposition Efficiencies

Moreover, the individual DEs for tungsten and steel were investigated each. They were found to deviate from the rule of mixture as reported for Ni and Ti in (Ref 20). In most cases, the best DEs of tungsten were found for the low tungsten content as well as for the higher gas temperature and pressure, Fig. 10. Two exceptional cases were observed with the coarse tungsten powder and the medium and high steel content (marked by arrows). Here, a stronger erosion of the steel matrix by the coarse tungsten particles might have occurred so that also some embedded tungsten particles were lost.

Regarding the DEs of steel, in all cases the best values were found for the higher gas temperature and pressure, Fig. 11. For the medium steel content, the steel DEs were best for both tungsten powders and also for the high steel content and the fine tungsten powder. The drop of DEs for

Fig. 10 Comparison of the tungsten DEs for the coarse and fine tungsten powder as well as for two gas temperatures and pressures; the uncertainty due to the limited resolution of the scale was estimated to be $< 0.03\%$ abs. DE



the coarse tungsten powder at the lowest content (marked with arrows) is assumed to be caused by the erosion of the steel matrix by the coarse tungsten particles.

Tungsten-Steel Ratios

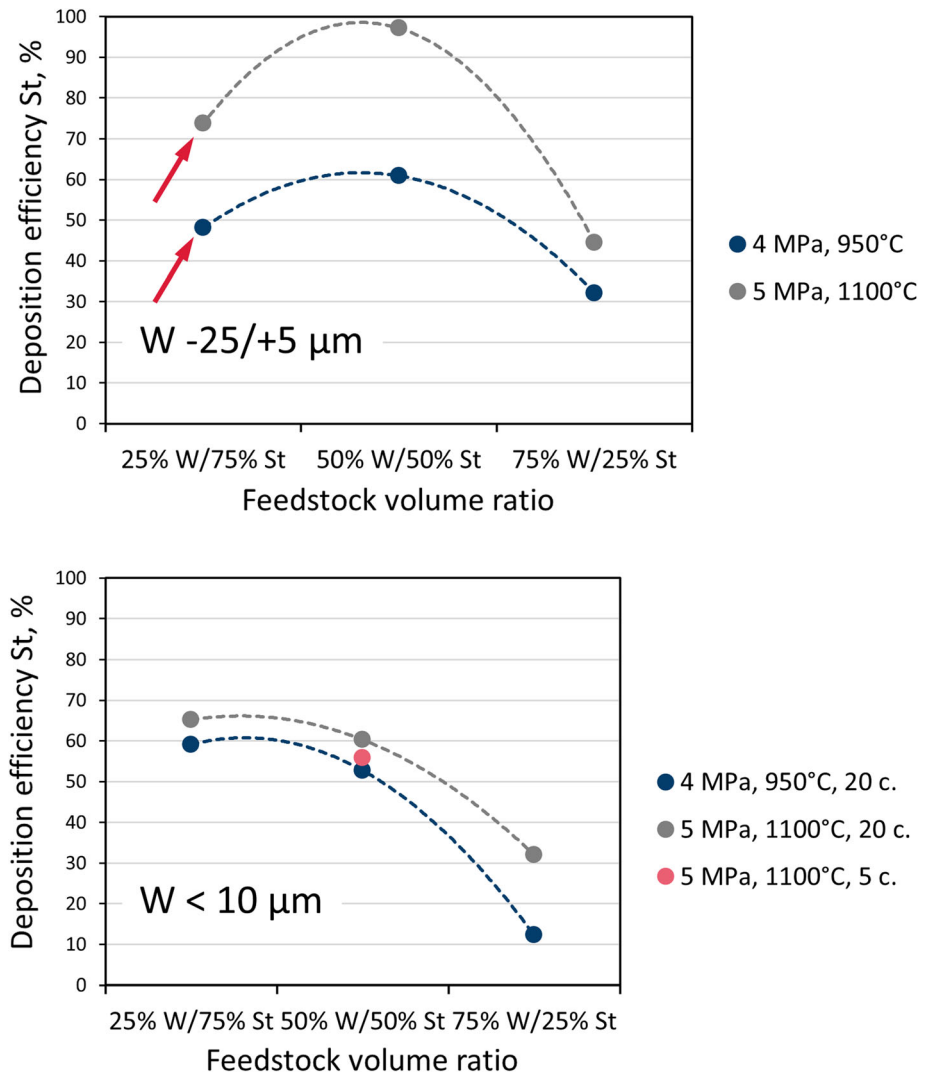
Figure 12 gives the percentages of cross-sectional area for tungsten, steel and pores as functions of the feedstock composition for the coarse and the fine tungsten powder as well as for two gas temperatures and pressures. It was mentioned above that the area fractions can be equate with the volume fractions. The following strategy to obtain a maximum tungsten content in the cold-sprayed coatings can be derived:

- In general, use the coarse tungsten powder ($-25/+5 \mu\text{m}$);
- For small and medium tungsten fractions, use lower gas temperature and pressure ($950^\circ\text{C}/4 \text{ MPa}$);

- For large tungsten fractions, use higher gas temperature and pressure ($1100^\circ\text{C}/5 \text{ MPa}$).

From Fig. 12, it is also obvious, that in none of the investigated cases the tungsten-steel ratio in the coatings is the same as the feedstock composition. The deviation increases as the tungsten content is raised due to the very different DEs of the both materials. Similar observations were reported for cold gas-sprayed tungsten-copper coatings. Kang et al. used an agglomerated composite feedstock with 75 wt.% tungsten and 25 wt.% copper and found that almost 38% of the tungsten was lost during spraying (Ref 21). Hall et al. processed copper-cladded tungsten powder with three different compositions. In all cases, the cold-sprayed deposits contained less tungsten than the feedstock. Using a powder with 80 wt.% tungsten, the content in the coating was 57 wt.%. It was suggested that tungsten was lost during the cold spray process as indications of the separation of copper and tungsten were found

Fig. 11 Comparison of the steel DEs for the coarse and fine tungsten powder as well as gas temperature and pressure; the uncertainty due to the limited resolution of the scale was estimated to be $< 0.08\%$ DE



(Ref 22). This means that the DEs of both materials must have been significantly different.

Oxidation

Inspecting SEM images at high magnification, some indications of a possible oxidation on the surfaces of steel particle were found. Figure 13 shows an example sprayed with 25% fine tungsten and 75% steel powder at 950 °C and 4 MPa. Some steel particles possibly showed indications of very slight oxidation at the surface. However, this could not be proved reliably by EDS as the size of the excitation bulb is much larger than the thickness of the supposed oxide layer. The XRD diffractograms (not shown) did not reveal any indication of the presence of oxides. There was also no evidence on the formation of undesired intermetallic Fe-W phases.

Conclusions

Tungsten-steel composite coatings could be successfully manufactured by cold gas spraying. Very dense coatings virtually free from oxidation and undesired intermetallic phases could be achieved at considerable DEs. The following conclusions on the governing deposition mechanisms can be drawn:

- Erosion exceeded the deposition rate when spraying 100% tungsten feedstock.
- When spraying tungsten-steel blends, the coarse tungsten powder was overall advantageous.
- A peening effect apparently occurred, which was naturally more pronounced with the coarser tungsten powder and at the higher pressure and temperature. This affected the porosity and the DE positively.
- The tungsten particles apparently also caused erosion affecting the DEs and the tungsten-steel ratio in the

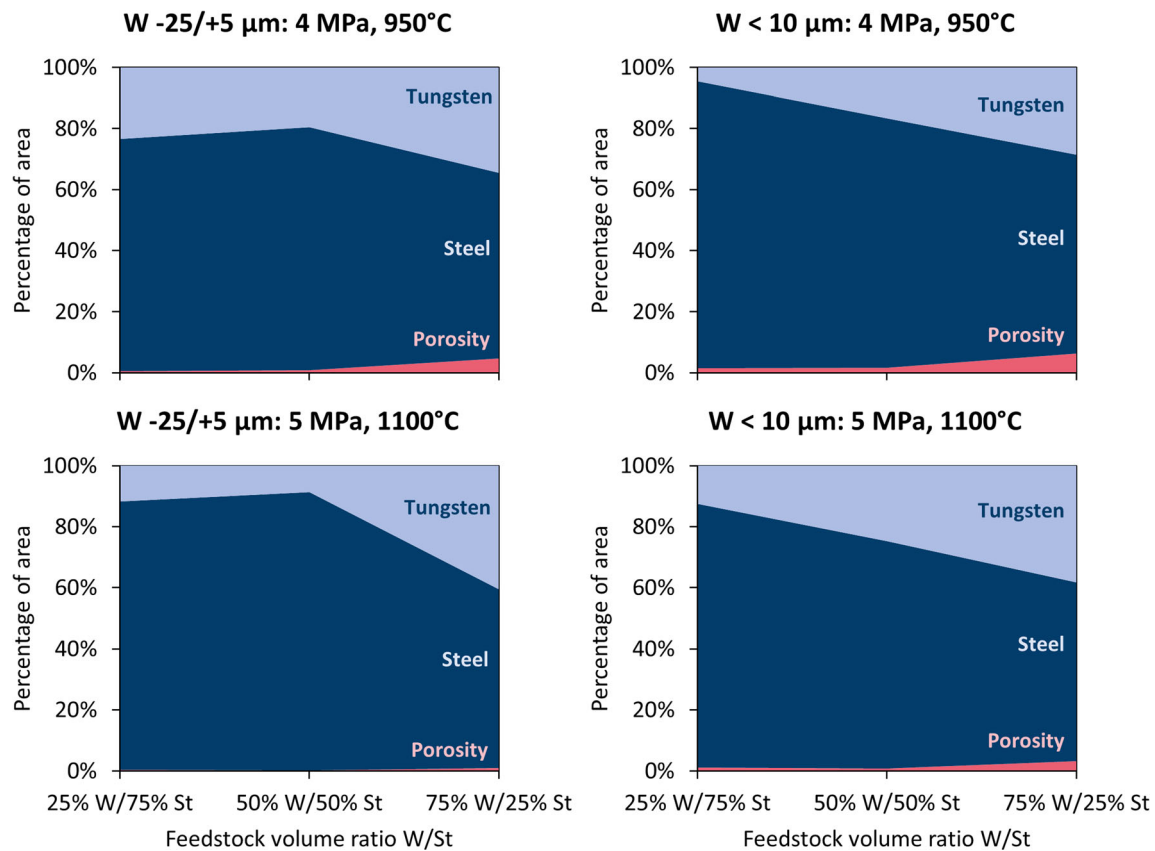


Fig. 12 Percentages of cross-sectional area for tungsten, steel and pores as functions of the feedstock composition for the coarse and the fine tungsten powder as well as different gas temperatures and pressures

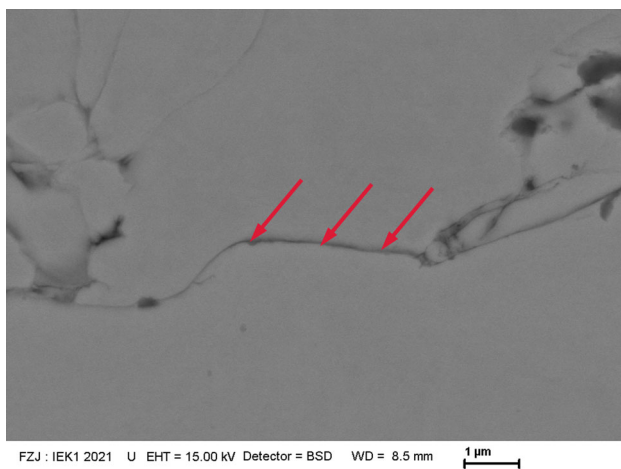


Fig. 13 Coating microstructure at high magnification (back-scattered electron image) of a coating sprayed with 25% fine tungsten and 75% steel powder at 950 °C and 4 MPa; the arrows indicate the surface of a steel particle possibly showing indications of very slight oxidation

coating. Obviously, the erosive attack first started at the steel matrix, before tungsten particles were then released from the surface. The erosive removal was greater with the coarser tungsten powder.

- Due to the very different nature of tungsten and steel (brittle vs. ductile) and the interactions to be assumed between the two materials affecting the deformation and deposition behavior, there was no sharply defined window of deposition; bonding, peening, and erosion effects apparently overlapped.

Furthermore, this work showed also that digital image analysis is a useful tool, provided that.

- The sample is representative of the workpiece;
- The microstructure is isometric, i.e., independent on position and orientation in the workpiece;
- The image quality is sufficient (resolution, no shading, etc.);
- The investigated microstructural components show a sufficiently large contrast;
- The statistical uncertainty of *observed* data can be estimated based on a sufficient number of images while the statistical uncertainty of *calculated* data can be assessed applying the laws of error propagation.

Acknowledgment The authors gratefully acknowledge Dr. Daniel Dorow-Gerspach and Dr. Simon Heuer (Forschungszentrum Jülich GmbH, IEK-4) for fruitful discussions and providing the fine tungsten

powder, Dr. Hanna V. Heyl for the topographic measurements, as well as Dr. Doris Sebold and Beatrix Göths for carrying out the SEM work (all Forschungszentrum Jülich GmbH).

Funding Open Access funding enabled and organized by Projekt DEAL.

Open Access This article is licensed under a Creative Commons Attribution 4.0 International License, which permits use, sharing, adaptation, distribution and reproduction in any medium or format, as long as you give appropriate credit to the original author(s) and the source, provide a link to the Creative Commons licence, and indicate if changes were made. The images or other third party material in this article are included in the article's Creative Commons licence, unless indicated otherwise in a credit line to the material. If material is not included in the article's Creative Commons licence and your intended use is not permitted by statutory regulation or exceeds the permitted use, you will need to obtain permission directly from the copyright holder. To view a copy of this licence, visit <http://creativecommons.org/licenses/by/4.0/>.

References

1. M. Claessens, ITER: The Giant Fusion Reactor: Bringing a Sun to Earth, 1st ed., Copernicus, 2020
2. D.J. Campbell, T. Akiyama, R. Barnsley, M. Bassan, L.R. Baylor, L. Bertalot, F. Escourbiac et al., Innovations in Technology and Science R&D for ITER, *J. Fusion Energy*, 2019, **38**(1), p 11-71.
3. M. Merola, F. Escourbiac, A.R. Raffray, P. Chappuis, T. Hirai and S. Gicquel, Engineering challenges and development of the ITER Blanket System and Divertor, *Fusion Eng. Des.*, 2015, **96–97**, p 34-41.
4. C. Linsmeier, M. Rieth, J. Aktaa, T. Chikada, A. Hoffmann, J. Hoffmann, A. Houben, H. Kurishita, X. Jin, M. Li, A. Litnovsky, S. Matsuo, A. von Müller, V. Nikolic, T. Palacios, R. Pippan, D. Qu, J. Reiser, J. Riesch, T. Shikama, R. Stieglitz, T. Weber, S. Wurster, J.H. You and Z. Zhou, Development of advanced high heat flux and plasma-facing materials, *Nucl. Fusion*, 2017, **57**(9), p 092009.
5. K. Mergia and N. Boukos, Structural, thermal, electrical and magnetic properties of Eurofer 97 steel, *J. Nucl. Mater.*, 2008, **373**(1), p 1-8.
6. A. Kohyama, A. Hishinuma, D.S. Gelles, R.L. Klueh, W. Dietz and K. Ehrlich, Low-activation ferritic and martensitic steels for fusion application, *J. Nucl. Mater.*, 1996, **233–237**, p 138-147.
7. Q. Huang, N. Baluc, Y. Dai, S. Jitsukawa, A. Kimura, J. Konys, R.J. Kurtz, R. Lindau, T. Muroga, G.R. Odette, B. Raj, R.E. Stoller, L. Tan, H. Tanigawa, A.A.F. Tavassoli, T. Yamamoto, F. Wan and Y. Wu, Recent progress of R&D activities on reduced activation ferritic/martensitic steels, *J. Nucl. Mater.*, 2013, **442**, p S2–S8.
8. J. Matějček, M. Vilémová, B. Nevrlá, L. Kocmanová, J. Veverka, M. Halasová and H. Hadraba, The influence of substrate temperature and spraying distance on the properties of plasma sprayed tungsten and steel coatings deposited in a shrouding chamber, *Surf. Coat. Technol.*, 2017, **318**, p 217-223.
9. J. Matějček, T. Kavka, G. Bertolissi, P. Ctibor, M. Vilémová, R. Mušálek and B. Nevrlá, The role of spraying parameters and inert gas shrouding in hybrid water-argon plasma spraying of tungsten and copper for nuclear fusion applications, *J. Therm. Spray Technol.*, 2013, **22**(5), p 744-755.
10. S. Heuer, J. Matějček, M. Vilémová, M. Koller, K. Illkova, J. Veverka, T. Weber, G. Pintsuk, J.W. Coenen and C. Linsmeier, Atmospheric plasma spraying of functionally graded steel/tungsten layers for the first wall of future fusion reactors, *Surf. Coat. Technol.*, 2019, **366**, p 170-178.
11. J. Matějček, T. Kavka, R. Mušálek, P. Ctibor, J. Medřický, M. Vilémová, B. Nevrlá, S. Degot and A. Denoirjean, Tungsten-steel composites and FGs prepared by argon-shrouded plasma spraying, *Surf. Coat. Technol.*, 2021, **406**, 126746.
12. T. Emmerich, D. Qu, R. Vaßen and J. Aktaa, Development of W-coating with functionally graded W/EUROFER-layers for protection of first-wall materials, *Fusion Eng. Des.*, 2018, **128**, p 58-67.
13. T. Emmerich, D. Qu, B.-E. Ghidersa, M. Lux, J. Rey, R. Vaßen and J. Aktaa, Development progress of coating first wall components with functionally graded W/EUROFER layers on laboratory scale, *Nucl. Fusion*, 2020, **60**(12), p 126004.
14. R. Vaßen, K.H. Rauwald, O. Guillon, J. Aktaa, T. Weber, H.C. Back, D. Qu and J. Gibmeier, Vacuum plasma spraying of functionally graded tungsten/EUROFER97 coatings for fusion applications, *Fusion Eng. Des.*, 2018, **133**, p 148-156.
15. M.F. SMITH, Comparing cold spray with thermal spray coating technologies, *The Cold Spray Materials Deposition Process*. Elsevier, 2007, p 43-61. <https://doi.org/10.1533/9781845693787.1.43>
16. J. Cizek, M. Vilemova, F. Lukac, M. Koller, J. Kondas and R. Singh, Cold sprayed tungsten armor for tokamak first wall, *Coatings*, 2019, **9**(12), p 836.
17. M.A. Delesse, *Procédé Mécanique Pour Déterminer la Composition Des Roches*, 3ème ed., F. Savy, Ed., La Société Géologique de France, 1866
18. H.E. Exner, H.P. Hougardy, *Einführung in Die Quantitative Gefügeanalyse*, Deutsche Gesellschaft für Metallkunde, 1986
19. W. Rasband, ImageJ, National institutes of health, 2022
20. R. Nikbakht, H. Assadi, K. Jahani, M. Saadati and B. Jodoin, Cold spray deformation and deposition of blended feedstock powders not necessarily obey the rule of mixture, *Surf. Coat. Technol.*, 2021, **424**, 127644.
21. H.-K. Kang and S.B. Kang, Tungsten/copper composite deposits produced by a cold spray, *Scr. Mater.*, 2003, **49**(12), p 1169-1174.
22. A.C. Hall, P. Sarobol, D.A. Urrea, S.S. Miller, Deposition behavior in cold sprayed copper-tungsten metal matrix composites (No. SAND2015-0115C), Sandia National Laboratories, 2015

Publisher's Note Springer Nature remains neutral with regard to jurisdictional claims in published maps and institutional affiliations.